On the parametrizations for the dissipation rate of the turbulence kinetic energy in stable conditions

Published Version:
Mario Schiavon, F.B. (2023). On the parametrizations for the dissipation rate of the turbulence kinetic energy in stable conditions. BULLETIN OF ATMOSPHERIC SCIENCE AND TECHNOLOGY, 4(1), 1-16 [10.1007/s42865-023-00055-6].

Availability:
This version is available at: https://hdl.handle.net/11585/925919 since: 2024-01-02

Published:
DOI: http://doi.org/10.1007/s42865-023-00055-6

Noname manuscript No.
(will be inserted by the editor)

On The Parametrizations for the Dissipation Rate of the Turbulence Kinetic Energy in Stable Conditions

Mario Schiavon · Francesco Barbano · Luigi Brogno · Laura Sandra Leo · Francesco Tampieri · Silvana Di Sabatino

Received: DD Month YEAR / Accepted: DD Month YEAR

Abstract
Observations acquired in the stable surface layer during two field experiments (The Mountain Terrain Atmospheric Modeling and Observations Program and the Climate Change Tower Integrated Project) are considered to test different parametrizations of the dissipation rate of turbulence kinetic energy (TKE). Particular attention is dedicated to the effect of the submeso motions on these parametrizations. The analysis shows that TKE-based formulations are particularly prone to the submeso effect, whilst better results are obtained if the vertical velocity variance is considered. In the latter case, stability must be taken into account explicitly in Mellor-Yamada type parametrizations but not in shear-based formulations.

Keywords Energy dissipation rate · Stable surface layer · Shear-based parametrizations · Submeso motions · Vertical velocity variance

1 Introduction

The viscous dissipation rate of turbulence kinetic energy (TKE), ϵ, is a key variable for turbulence models because it is a fundamental term in the TKE budget equation (Chamecki et al. 2018). Theoretically, this equation may be used to derive turbulence characteristics under simplifying assumptions, such

Corresponding author: M. Schiavon
Independent
E-mail: mario.skiavon@gmail.com

F. Barbano · L. Brogno · L. S. Leo · S. Di Sabatino
Univerity of Bologna, Department of Physics and Astronomy, Bologna, Italy

F. Tampieri
National Research Council, Institute of Atmospheric Sciences and Climate (CNR-ISAC), Bologna, Italy

as steadiness, horizontal homogeneity, and negligible third-order terms (Zilitinkevich et al. 2013). Practically, it is solved numerically in many weather, climate, and oceanic models to predict the TKE which, in turn, is used in other parametrizations of the model (e.g., to compute eddy viscosity and diffusivity).

Direct calculation of ϵ is rarely performed both in numerical and experimental studies due to the small spatial and temporal scales characterizing turbulence dissipation. This requires very high-frequency sample rates from the experimental instrumentation or fine-grid direct numerical simulations (DNS) solvers which are typically expensive and exceed the available computational resources for many applications. More often, indirect estimations of ϵ are obtained from velocity spectra and structure functions by using Kolmogorov's law (Kolmogorov 1941), but even these solutions may not be convenient for practical applications. Thus, significant work has been made to parametrize ϵ in terms of easily measurable characteristics of the flow, such as the TKE and the vertical velocity variance. Among the first and most recognized, Mellor and Yamada (1982) developed a TKE-based parametrization which is still used in numerical models and subject of investigation for more precise quantification of its parameters (see Sect. 2). On the other hand, Chen (1974) showed the proportionality of ϵ with the cube power of the vertical velocity variance, while Weinstock (1981) suggested the implication of buoyancy. Recently, Basu et al. (2021) reviewed these parametrizations by using DNS data and proposed new shear-based formulations which should portray quasi-universal scaling.

Whereas flow conditions and driving mechanisms may be controlled in numerical simulations, the atmospheric flow is perturbed by a variety of phenomena whose effect is not fully understood. Among these phenomena there are submeso motions. This term is used mainly in relation to the stable boundary layer (SBL) and refers to all motions with scale smaller than the meso-γ scale (about 2 km in the atmosphere) and larger than the scale of the main turbulent eddies (about $0.1z$, with z distance from the ground) (Mahrt 2014). However, a clear spectral gap between submeso motions and turbulent eddies often does not exist, making this separation somewhat arbitrary. In the time domain, where most observational analyses are carried out, submeso motions have scales shorter than ≈ 1 hr (Mortarini et al. 2013).

Submeso motions are ubiquitous in the atmosphere and associated with various phenomena, such as gravity waves, inertial oscillations, and drainage flows (Kang et al. 2014). Although these motions are always present, their effect is more evident in weak-wind conditions (Anfossi et al. 2005), which characterize the SBL. Study the submeso effect is thus crucial to address the SBL long standing questions concerning both theory and practical applications. With respect to the latter, submeso motions are among those boundary-layer processes that hinder contemporary numerical weather-prediction (NWP) models (Calaf et al. 2022).

Close to the ground, submeso motions appear as a low-frequency contribution to horizontal velocity fluctuations leading to strong turbulence anisotropy (Mortarini et al. 2019) that alters the amount of energy and momentum at the surface (Barbano et al. 2022). This contribution is not accounted for in the most common formulations for ϵ.

This study faces the same question of Basu et al. (2021), i.e., the validation of different parametrizations for ϵ, but using tower micrometeorological observations. These observations were acquired in the stable surface-layer during two field experiments and are hence characterized by the presence of submeso motions. The considered formulations are thus tested in the non-ideal condition of a perturbed flow. In particular, the study verifies whether

- without filtering the submeso contribution, formulations based on the vertical velocity variance are more robust than TKE-based parametrizations;
- in the stable atmospheric surface layer, shear-based parametrizations (Basu et al. 2021) performs differently from Mellor-Yamada formulations (Mellor and Yamada 1982).

The organization of the paper is as follows. Section 2 discusses the link between spectra and ϵ and reviews the formulations for ϵ considered in this study. In Sect. 3, the two experiments and the corresponding datasets analyzed in this study are described, along with the method used to estimate ϵ from the spectra. In Sect. 4, the observed characteristics of velocity spectra are discussed in relation to the addressed problem. In Sect. 5, the considered parametrizations for ϵ are tested by using observations from the two experiments. Conclusions are drawn in Sect. 6.

2 Theoretical Framework

It is common in turbulence research to partition each variable into mean and turbulent parts and consider a reference system with the x-axis aligned with the mean flow (Stull 1988). The velocity vector is thus written as $(U+u', v', w')$, where U is the mean flow velocity (modulus) and u', v', and w' are the streamwise, lateral, and vertical velocity fluctuations, respectively. By definition, $\overline{u'} = \overline{v'} = \overline{w'} = 0$, where the overbar denotes Reynolds average. The variances of the three velocity components are $\overline{u'^2} \equiv \sigma_u^2$, $\overline{v'^2} \equiv \sigma_v^2$, and $\overline{w'^2} \equiv \sigma_w^2$ and the TKE is $E_K \equiv (\sigma_u^2 + \sigma_v^2 + \sigma_w^2)/2$.

In the atmospheric surface layer, the varying stability may be accounted for by the Obukhov length, L (Tampieri 2017). In particular, $L \equiv -(\Theta/g)(u_*^3/\overline{w'\theta'})$, where g is gravitational acceleration, $\overline{w'\theta'}$ is the kinematic vertical turbulent heat flux (θ' is the turbulent temperature fluctuation), $u_* \equiv [\overline{u'w'}^2 + \overline{v'w'}^2]^{1/4}$ is friction velocity, and Θ is mean temperature (the minus sign provides $L > 0$ in the SBL).

To model turbulence behaviour, an important role is played by the power spectrum of the three velocity components, $E_\alpha(k)$, which gives the variance associated to each wavenumber k. In particular (Tampieri 2017)

$$\int_0^\infty E_\alpha(k)dk = \sigma_\alpha^2 \tag{1}$$

where k is the wavenumber in the steam-wise direction ($k = 2\pi f/U$, with f frequency in Hz), $\alpha = u, v, w$ represents the stream-wise, lateral, and vertical velocity component, and σ_α^2 its variance.

An integral length scale, l_α, may be defined and related to the value of the spectrum for $k = 0$ (Tampieri 2017):

$$l_\alpha \equiv \frac{\pi}{2\sigma_\alpha^2} E_\alpha(0) \tag{2}$$

Furthermore, given an analytical expression for the power spectrum $E_\alpha(k)$, a relation among the variance, σ_α^2, the TKE viscous dissipation rate, ϵ, and the integral length scale, l_α, may be obtained. For instance, by using (Olesen et al. 1984; Kaimal and Finnigan 1994)

$$E_\alpha(k) = \frac{C_\alpha \epsilon^{2/3}}{(b_\alpha^{-1} + k)^{5/3}} \tag{3}$$

where $C_u = 0.55$, $C_{v,w} = (4/3)C_u$, and $b_\alpha \equiv 3l_\alpha/\pi$, it results from Eq. (2) that

$$\epsilon = \left(\frac{2}{3C_\alpha}\right)^{3/2} \frac{\sigma_\alpha^3}{b_\alpha}. \tag{4}$$

For $k \gg b_\alpha^{-1}$, i.e., in the inertial subrange, Eq. (3) follows Kolmogorov's law (Kolmogorov 1941),

$$E_\alpha(k) = C_\alpha \epsilon^{2/3} k^{-5/3} \tag{5}$$

and $E_\alpha(k)$ becomes independent of the integral length scale l_α.

Often, spectra observed within the atmospheric boundary layer do not follow Eq. (3) or similar formulations, showing instead higher values in the low-k range (Andreas and Paulson 1979; Cava et al. 2001; Mortarini et al. 2016, e.g). This occurs when the flow is perturbed by submeso motions which, close to the surface, manifest as a low-wavenumber contribution to u and v spectra (Mortarini et al. 2013; Mahrt 2014), whilst the vertical velocity component is almost unaffected (Sect. 4). Alternative spectral models accounting for these small-k modes may be formulated. For instance, Mortarini and Anfossi (2015) proposed a spectral model that is suitable for low-wind/meandering conditions and other modifications may account for gravity waves.

By modifying the spectra, submeso motions affect the validity of Eqs. (3) and (4) and thus the possibility to find quasi-universal relationships between ϵ and the integral parameters (σ_α and l_α). Alternatively, in presence of low-k modes not related to ϵ, only the high-k part of the spectrum, Eq. (5), may be considered (Chen 1974). However, this requires the case-by-case determination of the inertial subrange extension, which is possible but not always easy (Falocchi et al. 2019).

Because time records are considered in this study, time scales instead of length scales – and frequencies instead of wavenumbers – are used hereafter. From dimensional considerations, the viscous dissipation may be written as

$$\epsilon = \frac{\upsilon^2}{T} \tag{6}$$

where υ is a velocity scale and T is the dissipation time scale (e.g., Zilitinkevich et al. 2013). Taking $T \sim l_\alpha/\upsilon$ and $\upsilon = \sigma_\alpha$, Eq. (6) reduces to Eq. (4). Different parametrizations are thus characterized by different velocity- and time-scales. If submeso motions are not relevant, the normalized spectrum depends only on stability (Kaimal et al. 1972) and the same occurs for length- or time-scales. However, if submeso motions are present the involved scales may depend on other parameters.

The widely used approach by Mellor and Yamada (1982) takes as velocity scale $\upsilon = q$, where $q^2 \equiv 2E_K$, and prescribes $T = Bl/q$, where l is a length scale related to the size of the main eddies and B is an empirical constant, with value varying among authors in the range $B \approx 12 - 24$ (Mellor and Yamada 1982; Nakanishi 2001; Nakanishi and Niino 2009; Wilson and Venayagamoorthy 2015; Basu et al. 2021). With this choice, Eq. (6) becomes

$$\epsilon = \frac{q^2}{Bl} \tag{7}$$

In the near-neutral surface layer, a common solution is $l = \kappa z$, being z the distance from the surface and $\kappa = 0.4$ the von Kármán constant. Furthermore, accounting for stablility (Cheng et al. 2020):

$$l = \frac{\kappa z}{1 + \alpha_1 z/L} \ , \ 0 < z/L < 1 \tag{8}$$

where L is the Obukhov length and $\alpha_1 = 2.7$. According to Nakanishi and Niino (2009), the length scale l may be limited to a stability-independent value for $z/L > 1$.

Basu et al. (2021) use both $E_K^{1/2}$ and σ_w as velocity scales, and the inverse of the mean velocity shear as time scale, i.e., $T \propto [\mathrm{d}U/\mathrm{d}z]^{-1}$ (by assuming no directional shear in the surface-layer), leading to the relationships

$$\epsilon = c_E E_K \frac{dU}{dz}, \quad \text{with} \quad c_E = 0.23 \tag{9}$$

and

$$\epsilon = c_w \sigma_w^2 \frac{dU}{dz}, \quad \text{with} \quad c_w = 0.63 \tag{10}$$

For a log-linear velocity profile, i.e., for $dU/dz = u_*(1 + \alpha_2 z/L)/(\kappa z)$, with u_* friction velocity and $\alpha_2 \approx 5$, (e.g., Högström 1996), Eqs. (9) and (10) may be rewritten similarly to Eq. (7), i.e., in terms of a length scale like that of Eq. (8) and the ratios E_K/u_*^2 or σ_w^2/u_*^2. For instance, from (9) we obtain

$$\epsilon = \frac{q^3}{B'l} \tag{11}$$

where $l = (\kappa z)/(1+\alpha_2 z/L)$, similar to Eq. (8), and $B' \equiv (2/c_E)(q/u_*) \approx 20$ in near-neutral conditions (by taking $q/u_* \approx 2$, see, e.g., Tampieri 2017), which compares with the values of B used in Eq. (7). Thus, if the velocity profile is log-linear, Eqs. (7), (9), and (10) are equivalent. However, whereas Mellor-Yamada formulation (Eq. 7) requires the specification of the length scale and its stability dependence, shear-based formulations (Eqs. 9 and 10) do not.

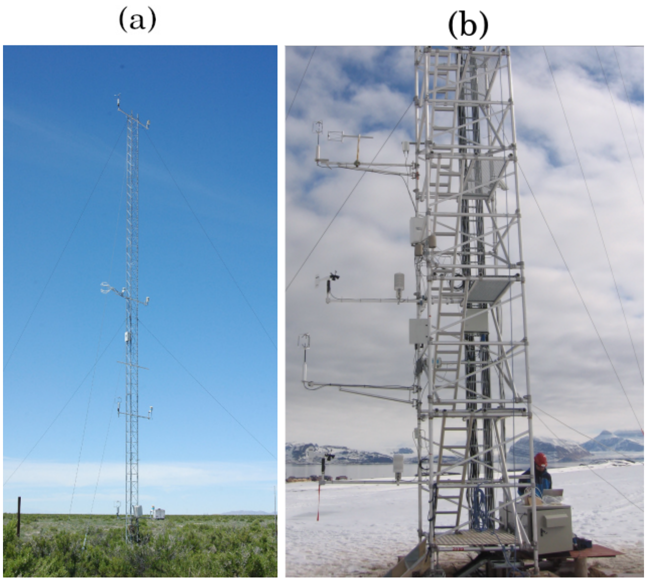

Fig. 1 Tower with intstrumental setup for (a) MATERHORN and (b) CCT-IP.

3 Observations

Observations from two field experiments are considered in this study: the Mountain Terrain Atmospheric Modeling and Observations (MATERHORN) Program and the Climate Change Tower Integrated Project (CCT-IP). The two datasets refer to tower observations acquired in the stable surface-layer. Because of the site characteristics, submeso activity is common in both experiments and thus ϵ formulations may be tested in conditions perturbed by these motions.

3.1 The Mountain Terrain Atmospheric Modeling and Observations Program

The Mountain Terrain Atmospheric Modeling and Observations Program (MATERHORN) dataset was assembled by using flux-tower measurement collected at the Dugway Proving Ground test-bed (Fernando et al. 2015). The gentle-sloping valley (with an average angle of $0.06°$ along the valley axis) is characterized by an arid soil heterogeneously covered by desert shrubs, located at 1300 m above mean sea level in South Utah. The valley floor is 40×30 km wide, surrounded by an isolated mountain peak (840 m) to the west and a mountain chain (peaks below 800 m) to the south, separated by a 5-km gap. The flux tower (Fig. 1a) was located at the field site of Sagebrush (40.121 360°N,113.129 070°W, altitude: 1316 m ASL) and equipped with 5 measurement levels (0.5 m, 2 m, 5 m, 10 m and 20 m) of sonic anemometers (81000, Young Company, Traverse

City, U.S.) sampling at 20 Hz, and temperature and relative-humidity probes (HMP45C-L, Campbell Scientific, Logan, U.S.) sampling at 1 Hz.

The dataset used for this investigation consists in the nocturnal periods of a set of weak-synoptic days occurred during Intensive Operational Periods (IOPs), i.e., days with the 700-hPa wind speed $U \leq 5\,\mathrm{ms}^{-1}$ (classified as quiescent IOPs, see Fernando et al. 2015) during fall 2012 and spring 2013. A total of 5 quiescent IOPs, namely IOP0, IOP1, IOP4, IOP7, and IOP8 (0,1, and 8, fall; 4 and 7, spring), compose the dataset (see Fernando et al. 2015 for a detailed description of them), characterized by a persistent low-level jet throughout the night and a continuous uptake of waves and intermittent turbulence arising close to the surface (Brogno et al. 2021).

To minimize unsteadiness, transitional periods across sunset and sunrise were removed. Therefore, the complex terrain heterogeneity and internal variability of the nocturnal boundary layer are expected to be the major source of perturbation for the boundary-layer flow. The collected data were preliminary processed to discard non-physical data. The sonic-anemometers measurements were further despiked using a data-removal procedure (Højstrup 1993) applied every 30-min data interval (Vickers and Mahrt 1997). The despiked wind components are then double-rotated to align the wind vector to the mean streamline direction (McMillen 1988). Second-order moments are then calculated as 30-min (co)variances.

3.2 Climate Change Tower Integrated Project

Two years (2012–2013) of observations from the Climate Change Tower Integrated Project (CCT-IP) are considered in this study (Mazzola et al. 2016).The Climate Change Tower (CCT) is 34 m high and equipped with fast- and slow-response instruments at several levels (Fig. 1b): mean velocity, temperature and humidity were measured with slow-response instruments at 2, 4.8, 10.3, and 33.4 m above the ground, whilst three sonic anemometers are placed at intermediate levels: 3.7, 7.5 (Gill R2 and R3, respectively, Lymington, Hampshire, UK) and 20.5 m (CSAT3, Campbell Scientific, Logan, U.S.). This study focuses on turbulence observation at the 7.5 m level, because, for technical reasons, few data are available from the other two levels during the considered period.

The experimental site is located in Ny-Ålesund (78°55′ N,11°55′ E), Svalbard, Norway, on the coast of Kongsfjorden, in an area with complex topography. The CCT is placed on a small relief (with height ≈ 50 m asl and horizontal scale ≈ 500 m), 2 km west to the Ny-Ålesund village and 1 km west to the Zeppelin mountain. Snow cover lasts from October to May whilst during the snow-free season, the ground is covered by stones and short grass, typical of arctic tundra. In this study, both snow-free and snow-covered conditions are considered without any distinction, because presented results do not differ for the two cases.

Raw data were divided into 30-min records. Sonic data, recorded at 20 Hz, were checked for spikes, plausibility limits and gaps. A double rotation was used to align the sonic reference system to the 30 min mean velocity. Second-order moments were calculated as 30-min (co)variances. To select stable conditions, only records with increasing temperature in the layer $2 - 10.3$ m and negative vertical fluxes of heat ($\overline{w'\theta'} < 0$) at $z = 7.5$ m are considered. Negative vertical fluxes of momentum ($\overline{u'w'} < 0$) at the same level and wind speed increasing in the same layer are also imposed, to guarantee shear production of TKE and obtain positive dissipations from Eqs. (9) and (10) which depend on the wind shear. Furthermore, wind directions in the range 150°–270° are excluded from the analysis to avoid flow distortion by the tower structure.

3.3 Estimation of the Dissipation Rate

For both datasets, the dissipation rate is obtained from the inertial subrange of the velocity spectra, Eq. (5). Because observations are acquired in the time domain, $S_\alpha(f)$ instead of $E_\alpha(k)$ is considered as the power spectra of the velocity component α as a function of the frequency f (measured in Hz), such that $fS_\alpha(f) = kE_\alpha(k)$ with $k = 2\pi f/U$ (Kaimal and Finnigan 1994), by assuming Taylor's hypothesis of frozen turbulence. This hypothesis may not hold under weak wind speed and significant submeso effect (Schiavon et al. 2019), thus breaking the link between f and k. However, this has no significant implications on the estimation of the dissipation rate, because a clear inertial subrange is always present in observed spectra (Sect. 4).

In particular, the dissipation rate is obtained from the high-frequency part of the u spectrum, because, having the longest inertial subrange, it gives the most reliable estimate of ϵ (Yadav et al. 1996). Thus,

$$\epsilon = \frac{2\pi}{U}\left[\frac{S_u(f)f^{5/3}}{C_u}\right]^{3/2}. \tag{12}$$

Starting from Eq. (12), different techniques were used for the two datasets, because of the different characteristics of the two experiments. For CCT-IP, the term in square brackets was averaged over the interval $2U/z < f < 4$ Hz, where the lower boundary corresponds the low-frequency end of the inertial subrange (e.g. Kaimal and Finnigan 1994), while $f < 4$ Hz avoids aliasing effects. Inertial-subrange isotropy was verified by calculating ϵ also from the v and w spectra and obtaining differences $< 10\%$.

For MATERHORN, ϵ is calculated by a linear regression of Eq. (12) in a frequency range estimated from the mean nocturnal spectra (Barbano et al. 2022): other techiques, including that used for CCT-IP, were tested for this dataset and gave similar results, thus indicating small sensitivity to the method. For both datasets, only records with at least four spectral points in the inertial subrange were retained.

4 Spectra

As discussed in Sect. 2, if an inertial subrange is present, the viscous dissipation rate, ϵ, is linked to the shape of the spectrum (Eq. 4). However, submeso motions modify the spectra in such a way that formulations like Eq. (3) are no longer valid. To account for these aspects, the spectra of the three velocity components for the considered datasets are analyzed in this section.

Figure 2 shows the observed spectra for the MATERHORN and CCT-IP experiments (the IOP1 from MATERHORN dataset is shown as an example due to the similar characteristics observed within the other IOPs). For CCT-IP, to isolate the submeso effect from the stability dependence, near-neutral conditions are selected, by imposing $0 < z/L < 0.05$ at $z = 7.5\,\mathrm{m}$ (the level considered in this study). Furthermore, CCT-IP spectra are separated according to wind-speed, which is related to the relative strength of submeso motions (Schiavon et al. 2019). MATERHORN spectra, instead, are presented for the five tower levels. By increasing z or decreasing U, small-scale turbulence intensity decreases and the relative strength of submeso motion increases. All spectra are anchored in the inertial subrange by taking $fS_\alpha(f)/(\kappa z\epsilon)^{2/3}$, with $\alpha = u, v, w$.

For comparison, Fig. 2 also shows the model suitable for no submeso contribution and near-neutral conditions (Olesen et al. 1984):

$$\frac{fS_\alpha(f)}{(\kappa z\epsilon)^{2/3}} = \frac{A_\alpha n}{(1 + B_\alpha n)^{5/3}} \tag{13}$$

where $\alpha = u, v, w$, $n = fz/U$ is the non dimensional frequency,

$$A_u = B_u^{5/3} C_u (2\pi\kappa)^{-2/3} \quad \text{and} \quad A_{v,w} = \frac{4}{3} B_{v,w}^{5/3} C_u (2\pi\kappa)^{-2/3}. \tag{14}$$

In particular, $A_u = 102$, $A_v = 17$, $B_u = 33$, and $B_v = 9.5$ are taken from the Kansas spectra (Kaimal and Finnigan 1994). To fit better the observations, a model different from Eq. (13) was used for the w spectrum in the Kansas experiment. For sake of simplicity, and because in this case Eq. (13) agrees well with observations (Fig. 2f), in this study Eq. (13) was used also for the vertical velocity component, with $A_w = 4.3$ and $B_w = 4.2$ obtained from previous analysis (Schiavon et al. 2019). Equations (13) and (3) are similar and thus relations exist among the corresponding parameters, i.e., $B_\alpha = b_\alpha(2\pi/z) = 6l_\alpha/z$.

As expected, submeso motions lead to completely different behaviours of horizontal velocity components (Figs. 2a-d) vs the vertical one (Figs. 2e,f). Indeed, contrary to the latter (Figs. 2e-f), horizontal velocity components are significantly affected by submeso motions (Figs. 2a-d) . In particular, two frequency ranges may be recognized. An high-frequency range, for $n \gtrsim 0.1$, where the observed spectra follow Eq. (13). A low frequency range, for $n \lesssim 0.1$, where the submeso contribution is dominant and spectral levels are higher than those predicted by Eq. (13). The high-frequency range is dominated by small-scale turbulence: for MATERHORN, the effect of increasing stability is visible

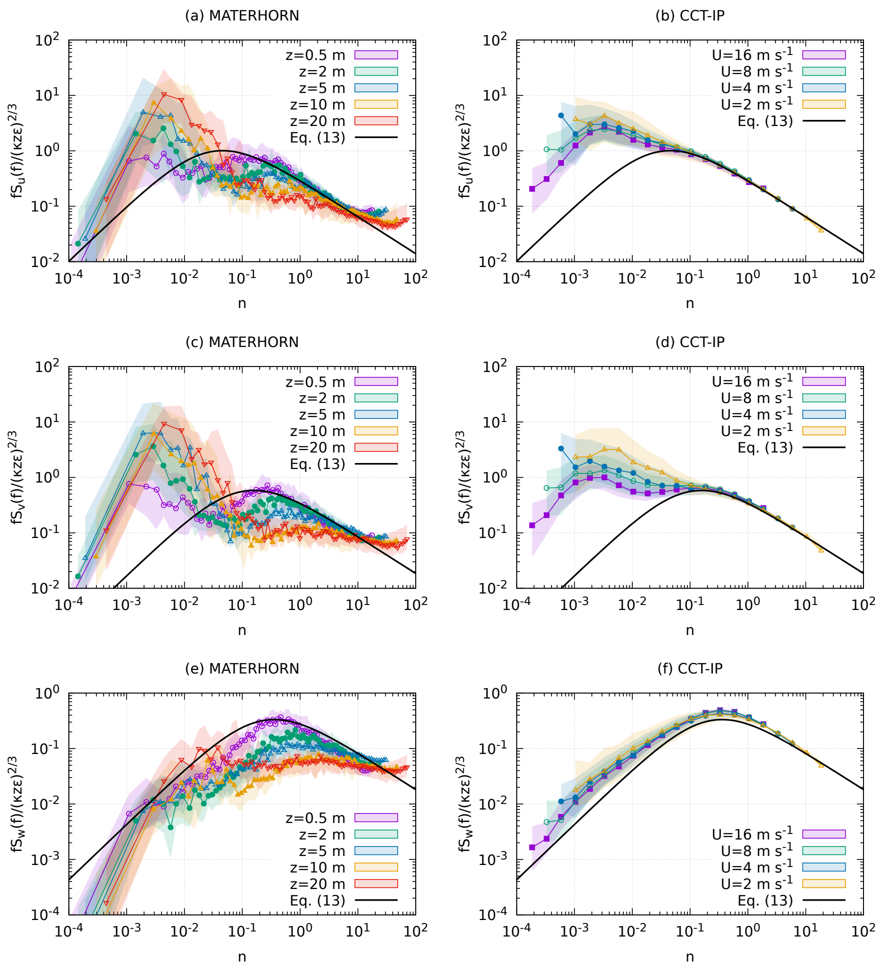

Fig. 2 Frequency weighted spectra, $fS_\alpha(f)$ (with $\alpha = u$, top; v, middle; and w, bottom), normalized by $(\kappa z \epsilon)^{2/3}$ vs the non-dimensional frequency $n = fz/U$ for the MATERHORN (left, IOP1) and CCT-IP dataset (right, $0 < z/L < 0.05$). MATERHORN spectra correspond to the height of the five tower levels, z. CCT-IP spectra correspond to $z = 7.5\,\mathrm{m}$ and different wind-speed intervals, each $2\,\mathrm{ms}^{-1}$ wide and centered around the reported value (U is wind speed at 7.5 m). Median values (points) and variability (shaded area, corresponding to the interquartile range) are shown for each level or U class. Eq. (13) is also represented for comparison

in this range through the decrease in the spectral levels with increasing height (taking the IOP1 average, z/L increases from ≈ 2.5 to ≈ 7 from $z = 0.5\,\mathrm{m}$ to $z = 20\,\mathrm{m}$). For CCT-IP, a clear inertial subrange is always observed, for $n \gtrsim 1$ (Figs. 2b, d, and f). For MATERHORN, the extension of this range shortens as the height increases because of the increasing stability: for the case shown in Figs. 2a,c, and e, small-scale turbulence is weak at $z = 10\,\mathrm{m}$ and $20\,\mathrm{m}$.

The observed submeso contribution may have different origins. All the considered IOPs of the MATERHORN dataset are characterized by wave activity. This is particularly evident by looking at the peak of the u and v spectra in the range $10^{-3} \lesssim n \lesssim 10^{-2}$ and at the spectral gap especially in the lowest levels (Figs. 2a,c): at $z = 0.5$ m (purple line) the gap is at $n \approx 0.1$ for the u component (Fig. 2a) and $n \approx 0.2$ for the v component (Figs. 2c). For the CCT-IP dataset, the nature of the submeso motions is less clear, with horizontal heterogeneity that is responsible of an intense and variable submeso activity. Within MATERHORN cases, some have been recognized as inertial-gravity waves induced by perturbations of the mean flow (Brogno et al. 2021; Barbano et al. 2022). In spite of these differences, the low-frequency peak for the CCT-IP spectra (Fig. 2b,d) is about at the same positions of the MATERHORN dataset (Fig. 2a,c). Although this similarity is interesting, the position and the magnitude of this peak should be considered with caution, because Taylor's hypothesis may be not fulfilled in weak wind conditions (Schiavon et al. 2019) and submeso scales may be poorly sampled, being close to the record length.

Whereas $(\kappa z \epsilon)^{2/3}$ is the adequate scale in the high-frequency range (with the exception of stability effects, all spectra collapse on the same curve for $n \gtrsim 0.1$), this is not the case for the submeso contribution ($n \lesssim 0.1$), whose relative magnitude increases with increasing height (Figs. 2a,c) or decreasing wind speed (Figs. 2b,d). This confirms the weak relation between the submeso contribution and viscous dissipation (the former does not scale with the latter, contrary to small-scale turbulence) and the need for other parameters related to submeso motions to describe the spectra in the low-frequency range. For these reasons, horizontal velocity variances, which show the highest submeso contribution, are expected to be inappropriate scales for ϵ.

Contrary to horizontal velocity components, vertical velocity spectra are almost unaffected by the submeso contribution, because large-scale vertical velocity fluctuations are damped close to the ground (Højstrup 1982). Thus the observed spectra closely follow Eq. (13). This is particularly evident for CCT-IP (Fig. 2f). The negligible submeso contribution to the w spectrum indicates that the vertical velocity variance is a suitable scale for ϵ, even in presence of submeso motions. Because these motions contribute to horizontal velocity components but not to the vertical one, larger anisotropy corresponds to stronger submeso effect (as discussed further in Sect. 5.1).

5 Results

The parametrizations discussed in Sect. 2 are tested with CCT-IP and MATERHORN data by taking into account the submeso effect. For MATERHORN, data from different IOPs and levels are considered together, because a similar behaviour is observed.

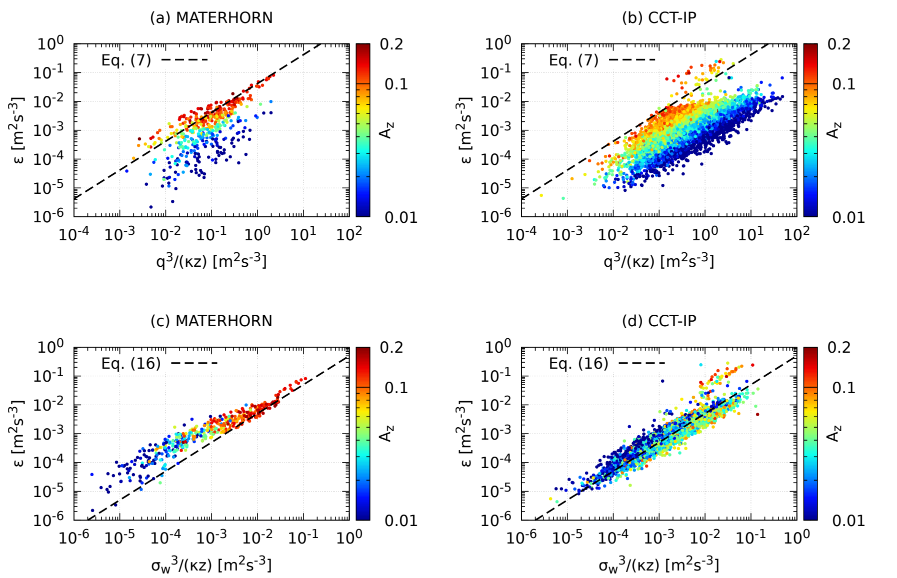

Fig. 3 Observed dissipation rate, ϵ, vs $q^3/(\kappa z)$ (top) and $\sigma_w^3/(\kappa z)$ (bottom) for MATERHORN (left) and CCT-IP (right). Each point corresponds to a 30-min record and is colored according to the anisotropy degree, A_z, Eq. (15). For comparison, Eqs. (7) and (16), with $l = \kappa z$, $B = 24$ and $B_w = 2$, respectively, are also represented.

5.1 Mellor-Yamada Type Parameterizations

Figures 3a-b show the observed dissipation rate, ϵ, vs $q^3/(\kappa z)$, which is the Mellor-Yamada-type parametrization, i.e., Eq. (7), without B and with $l = \kappa z$. To account for the strength of the submeso effect, data are stratified according to the anisotropy degree

$$A_z \equiv \frac{\sigma_w^2}{q^2} \tag{15}$$

which is the relative contribution to the TKE by the vertical velocity variance. Besides the fact that A_z has been used as a key parameter to model the turbulent flow (Zilitinkevich et al. 2013), its value is also related to the strength of the submeso effect (Mortarini et al. 2019; Schiavon et al. 2019, Sect. 4). In particular, A_z decreases (anisotropy increases) as the strength of submeso motions increases, because submeso motions are almost two-dimensional close to the ground.

Figures 3a-b show that observations dispose ordinately according to A_z, with smaller A_z (stronger submeso effect) corresponding to larger deviations from Eq. (7). In particular, for MATERHORN (Fig. 3a), Eq. (7) (with $l = \kappa z$) is approximately valid when $A_z \gtrsim 0.1$, returning $B = 0.24$ as a best fit, in line with Nakanishi (2001). Conversely, Eq. (7) over-predicts the observed dissipation for smaller A_z. The latter case always occurs for CCT-IP (Fig. 3b), for which $A_z < 0.1$ is generally observed (Schiavon et al. 2019). The overestimation of ϵ by using Eq. (7) is due to the submeso contribution to the TKE but not to ϵ, consistently with the behaviour of the low-frequency part of u and v spectra discussed in Sect. 4.

As shown in Sect. 4, the submeso contribution to the vertical velocity variance is negligible close to the ground. Thus, following Eq. (7), an alternative parametrization is considered by taking for the velocity scale σ_w:

$$\epsilon = \frac{\sigma_w^3}{B_w l}, \tag{16}$$

where, as in Eq. (7), B_w is an empirical constant and l is the length scale. This parametrization is tested in Figs. 3c-d by taking $l = \kappa z$ as in Figs. 3a-b. Contrary to Figs. 3a-b, data collapse on a single curve independently of A_z. This curve is close to Eq. (16) with $B_w = 2$, a value which corresponds to $B_w = BA_z^{3/2}$, by taking $B = 24$ and $A_z = 0.2$, consistently with the near-neutral reference value for A_z in absence of submeso contribution (Tampieri 2017; Schiavon et al. 2019). Thus Eq. (16) is more robust than Eq. (7) against the submeso effect and explains most of the observed variability in ϵ.

The deviation from the linear behaviour observed for MATERHORN for low values of $\sigma_w^3/(\kappa z)$ (Fig. 3c) is due to the stability dependence, which instead is negligible for the CCT-IP dataset (Fig. 3d). As discussed in Sect. 2, this effect is accounted for by considering a stability dependence of the length scale l. According to Eqs. (7) and (16), this stability dependence may be studied by considering the ratio between $\kappa z \epsilon$ and q^3 or σ_w^3. Following Eq. (8) and Nakanishi and Niino (2009), we expect that

$$\frac{\kappa z \epsilon}{q^3} = \begin{cases} (1 + \alpha_1 z/L)/B & \text{for } z/L \le 1 \\ (1 + \alpha_1)/B & \text{for } z/L > 1 \end{cases} \tag{17}$$

where $\alpha_1 = 2.7$ and B_w substitutes B if σ_w instead of q is considered.

Figure 4 shows the stability dependence of $\kappa z \epsilon$ divided by q^3 and σ_w^3. Equation (17) is also reported, with $B = 24$ and $B_w = 2$. As expected, the stability dependence is more clear if σ_w instead of q is used as a velocity scale. This is true for both datasets but is more evident for MATERHORN (compare Fig. 4a and c): when q is considered, only data with large A_z follow Eq. (17) (Fig. 4a), whereas, by using σ_w all data collapse around the expected relationship. With respect to MATERHORN, more scatter and a negligible stability dependence are observed for the CCT-IP dataset, even if σ_w is considered (Fig. 4c). Figures 4c-d also show that, on average, A_z decreases with increasing stability, consistently with other experiments (Zilitinkevich et al. 2013; Tampieri 2017). As observed in Fig. 3d, the stability dependence for CCT-IP is weak (Fig. 4d).

5.2 Shear-Based Parametrizations

Figure 5 shows shear-based parametrizations, both in terms of the TKE and the vertical velocity variance. Since the estimation of vertical gradients may

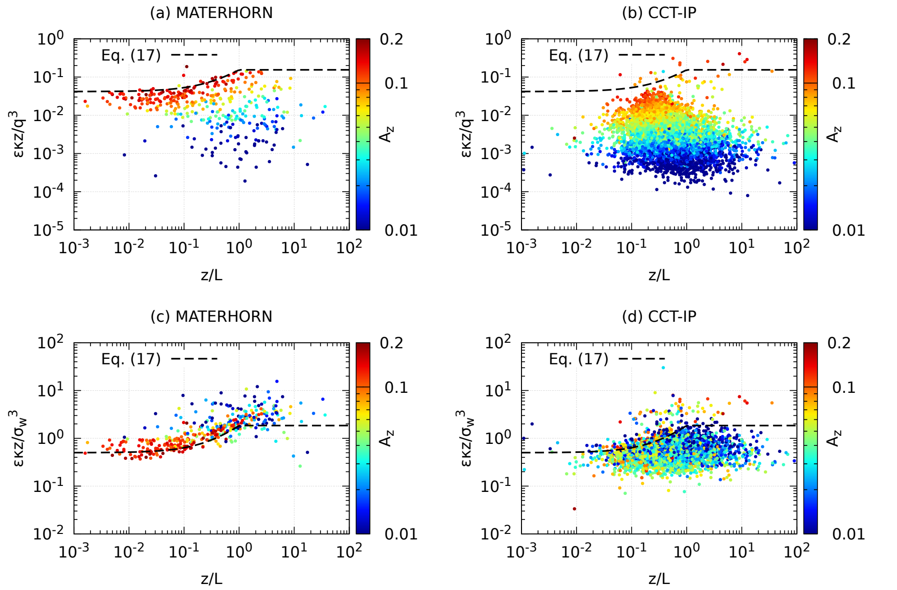

Fig. 4 Dependence on z/L of $\kappa z \epsilon$ divided by q^3 (top) and σ_w^3 (bottom) for MATERHORN (left) and CCT-IP (right). As in previous figures, data are colored according to A_z. Eq. (17), with $B = 24$ (top) and $B_w = 0.2$ (bottom) is also represented

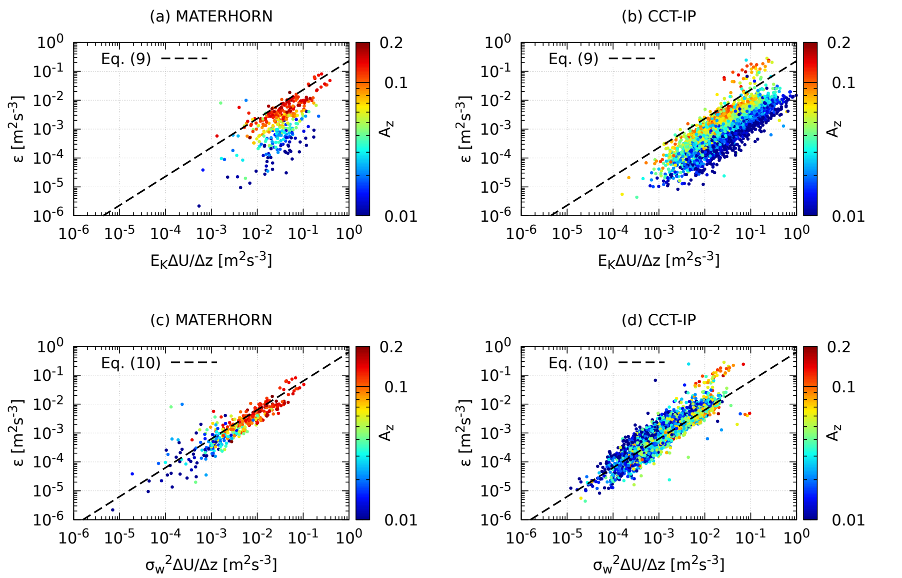

Fig. 5 Observed dissipation rate, ϵ, vs shear-based parametrizations: $E_K \Delta U/\Delta z$ (top) and $\sigma_w^2 \Delta U/\Delta z$ (bottom), for MATERHORN (left) and CCT-IP (right). As in previous figures data are colored according to A_z. Eqs. (9) and (10) are also represented

be sensitive to the method and may introduce further errors, their bulk formulation is considered, by taking the bulk wind shear $\Delta U/\Delta z$, instead of dU/dz: the two formulations are equivalent if ϵ and E_K or σ_w^2 are constant in the considered layer, which is a reasonable approximation close to the surface. Eqs. 9 and 10 are also plotted in Fig. 5 for reference. $\Delta U/\Delta z$ is calculated between 4.8 and 10.3 m for CCT-IP (i.e., the two levels that contain the sonic at $z = 7.5$ m), whilst the given sonic level and the sonic level above are used for MATERHORN (with the exception of the highest level, for which the level below is considered). These differences between datasets are due to different experimental setups and data availability (Sect. 3) and have a minor impact on the presented results.

For the considered datasets, concerning their robustness against the submeso effect, similar considerations apply for shear-based and Mellor-Yamada formulations (Sect. 5.1), confirming that the key factor is the choice of the velocity scale. Indeed, also shear-based parametrizations are unaffected by submeso motions if the vertical velocity variance, instead of the TKE, is used to define the velocity scale (compare Figs. 5a,b with Figs. 5c,d). However, the advantage of shear-based formulations is that no stability correction is necessary, because stability is embedded in the wind shear (compare Fig. 5c and Fig. 3c). The drawback is that, when the stability effect is negligible, as for CCT-IP, the calculation of the wind shear may introduce more scatter in the data (compare Fig. 3d and Fig. 5d).

6 Conclusions

Different parametrizations of the dissipation rate of turbulence kinetic energy (TKE) were validated with turbulence observations acquired in the atmospheric stable surface-layer during two field experiments. In particular, Mellor-Yamada type formulations (Mellor and Yamada 1982) and shear-based parametrizations (Basu et al. 2021) were considered, with velocity scale based on the unfiltered TKE and vertical velocity variance, σ_w^2. The flow was characterized by the presence of submeso motions. Particular attention was paid to the effect of these motions on the considered formulations.

Among all factors, the choice of the velocity scale was determinant for the robustness of the parametrization against the submeso effect. In particular, as expected, formulations based on σ_w were more robust than TKE-based parametrizations, because of the submeso contribution to horizontal velocity variances which is uncorrelated with dissipation. Hence, the dissipation rate is overestimated if TKE-based parametrizations are used in presence of submeso motions as often occurs in the atmosphere. Furthermore, TKE-based formulations cannot be universal, because of the high variability of the submeso contribution at the same place and among different places. Hence, close to the ground, the vertical velocity variance should be preferred on the TKE for the velocity scale of the dissipation rate.

This result is not in contrast with the good performance of TKE-based parametrizations observed in direct numerical simulations (Basu et al. 2021), because, in this case, only small-scale turbulence contributes to the TKE. This may suggest that a "filtered" TKE could be used also for the atmosphere. However, filtering out the submeso contribution from horizontal velocity variances is not always possible, because a clear spectral gap often does not exists. An alternative approach is to retain only inertial-subrange scales (Falocchi et al. 2019). Clearly, this would give the "right" TKE for the dissipation rate, but at the cost of a more difficult implementation, especially for practical applications. For this reason, in the surface layer, the use of the unfiltered σ_w may be more convenient. If the TKE is considered, different scales should be used for different applications: the small-scale TKE may be used in numerical weather prediction (NWP) models, whereas the submeso contribution is critical in dispersion models, to estimate the probability distribution function of the three velocity components. To compare results obtained in this study with large-eddy simulations (LES), the total TKE, i.e., that from resolved and unresolved scales, should be considered.

If σ_w is used for the velocity scale, Mellor-Yamada and shear-based parametrizations are equally good if a stability correction is applied to the former. The equivalence of these formulations is related to the link between the dissipation length scale and the wind shear given by the log-linear velocity profile.

In agreement with other studies (Mortarini et al. 2019; Schiavon et al. 2019), turbulence anisotropy degree was a useful parameter to identify the presence of submeso motions close to the ground.

Future research may focus on the link between these results and deeper aspects of the turbulent flow, that may be investigated by using spectral models accounting for the submeso contribution and by considering the effect of this contribution on the TKE budget. Because the dissipation rate is a key element of the TKE budget (Chamecki et al. 2018), the discussion about its parameterization is tied with understanding and interpreting the budget in actual, usually non-ideal, conditions.

7 Data Availability

Concerning the CCT-IP dataset, data generated and analysed in this study are available from M.S. with permission of the National Research Council, Institute of Polar Sciences (CNR-ISP).

Concerning MATERHORN dataset, data analyzed during the current study are available in the EOL data archive (`https://data.eol.ucar.edu`). This dataset was derived from the following public domain resource:MATERHORN data, `https://data.eol.ucar.edu/master_lists/generated/materhorn-x`.

8 Competing Interests

The authors have no competing interests to declare that are relevant to the content of this article.

Acknowledgements F.T. and M.S. thank the Department of Earth System Sciences and Technologies for the Environment of the National Research Council (CNR-DSSTTA) and its staff for the logistical support at the Arctic Station Dirigibile Italia in Ny-Ålesund and Drs. M. Mazzola e A. P. Viola for the collection and preliminar elaboration of the CCT-IP dataset. The authors acknowledge two anonymuos reviewers for their corrections and suggestions.

References

Andreas EL, Paulson C (1979) Velocity spectra and cospectra and integral statistics over arctic leads. Quartery Journal of the Royal Meteorological Society 105:1053–1070

Barbano F, Brogno L, Tampieri F, Di Sabatino S (2022) Interaction Between Waves and Turbulence Within the Nocturnal Boundary Layer. Boundary-Layer Meteorology DOI 10.1007/s10546-021-00678-2

Basu S, He P, DeMarco AW (2021) Parametrizing the Energy Dissipation Rate in Stably Stratified Flows. Boundary-Layer Meteorology 178:167–184

Brogno L, Barbano F, Leo LS, Fernando HJ, Di Sabatino S (2021) Driving mechanisms of double-nosed low-level jets during MATERHORN experiment. Journal of the Atmospheric Sciences 78(12):4037–4051

Calaf M, Vercauteren N, Katul GG, Giometto MG, Morrison TJ, Margairaz F, Boyko V, Pardyjak ER (2022) Boundary-layer processes hindering contemporary numerical weather prediction models. Boundary-Layer Meteorology pp 1–26

Cava D, Giostra U, Tagliazucca M (2001) Spectral maxima in a perturbed stable boundary layer. Boundary-layer meteorology 100(3):421–437

Chamecki M, Dias NL, Freire LS (2018) A TKE-Based Framework for Studying Disturbed Atmospheric Surface Layer Flows and Application to Vertical Velocity Variance Over Canopies. Geophysical Research Letters 45:6734–6740, DOI 10.1029/2018GL077853

Chen W (1974) Energy dissipation rates of free atmospheric turbulence. Journal of Atmospheric Sciences 31(8):2222–2225

Cheng Y, Canuto V, Howard A, Ackerman AS, Kelley M, Fridlind AM, Schmidt GA, Yao MS, Del Genio A, Elsaesser GS (2020) A Second-Order Closure Turbulence Model: New Heat Flux Equations and No Critical Richardson Number. Journal Of Atmospheric Sciences 77:2743–2759, DOI 10.1175/JAS-D-19-0240.1

Falocchi M, Giovannini L, de Franceschi M, Zardi D (2019) A method to determine the characteristic time-scales of quasi-isotropic surface-layer turbulence over complex terrain: A case-study in the Adige Valley (Italian Alps). Quarterly Journal of the Royal Meteorological Society 145(719):495–512

Fernando H, Pardyjak E, Di Sabatino S, Chow F, De Wekker S, Hoch S, Hacker J, Pace J, Pratt T, Pu Z, et al. (2015) The MATERHORN: Unraveling the intricacies of mountain weather. Bulletin of the American Meteorological Society 96(11):1945–1967

Högström U (1996) Review of some basic characteristics of the atmospheric surface layer. Boundary-Layer Meteorol 78:215–246

Højstrup J (1982) Velocity spectra in the unstable planetary boundary layer. Journal of the Atmospheric Sciences 39(10):2239–2248

Højstrup J (1993) A statistical data screening procedure. Measurement Science and Technology 4(2):153

Kaimal JC, Finnigan JJ (1994) Atmospheric boundary layer flows. Their structure and measurement. Oxford University Press

Kaimal JC, Wyngaard JC, Izumi Y, Coté OR (1972) Spectral characteristics of surface-layer turbulence. Quart J Roy Meteor Soc 98:563–589

Kang Y, Belušić D, Smith-Miles K (2014) Detecting and classifying events in noisy time series. Journal of the Atmospheric Sciences 71(3):1090–1104

Kolmogorov AN (1941) The local structure of turbulence in incompressible viscous fluid for very large Reynolds numbers. Dokl Akad Nauk SSSR 30:301

Mahrt L (2014) Stably stratified atmospheric boundary layers. Annu Rev Fluid Mech 46:23–45, DOI 10.1146/annurev-fluid-010313-141354

Mazzola M, Viola AP, Lanconelli C, Vitale V (2016) Atmospheric observations at the Amundsen-Nobile Climate Change Tower in Ny-Ålesund, Svalbard. Rendiconti Lincei 27(1):7–18

McMillen RT (1988) An eddy correlation technique with extended applicability to non-simple terrain. Boundary-Layer Meteorology 43(3):231–245

Mellor GL, Yamada T (1982) Development of a turbulence closure model for geophysical fluid problems. Reviews of Geophysics and Space Physics 20(4):851–875

Mortarini L, Anfossi D (2015) Proposal of an empirical velocity spectrum formula in low-wind speed conditions. Quarterly Journal of the Royal Meteorological Society 141(686):85–97

Mortarini L, Ferrero E, Falabino S, Trini Castelli S, Richiardone R, Anfossi D (2013) Low-frequency processes and turbulence structure in a perturbed boundary layer. Quarterly Journal of the Royal Meteorological Society 139(673):1059–1072

Mortarini L, Stefanello M, Degrazia G, Roberti D, Castelli ST, Anfossi D (2016) Characterization of wind meandering in low-wind-speed conditions. Boundary-Layer Meteorology 161(1):165–182

Mortarini L, Cava D, Giostra U, Costa FD, Degrazia G, Anfossi D, Acevedo O (2019) Horizontal meandering as a distinctive feature of the stable boundary layer. Journal of the Atmospheric Sciences 76(10):3029–3046

Nakanishi M (2001) Improvement of the mellor–yamada turbulence closure model based on large-eddy simulation data. Boundary-layer meteorology 99(3):349–378

Nakanishi M, Niino H (2009) Development of an improved turbulence closure model for the atmospheric boundary layer. Journal Meteorological Society

Japan 87:895–912

Olesen HR, Larsen SE, Hojstrup J (1984) Modelling velocity spectra in the lower part of the planetary boundary layer. Boundary-Layer Meteorol 29:285–312

Schiavon M, Tampieri F, Bosveld F, Mazzola M, Castelli ST, Viola A, Yagüe C (2019) The Share of the Mean Turbulent Kinetic Energy in the Near-Neutral Surface Layer for High and Low Wind Speeds. Boundary-Layer Meteorology 172:81–106

Stull RB (1988) An introduction to boundary layer meteorology. Kluwer Academic Publishers

Tampieri F (2017) Turbulence and dispersion in the planetary boundary layer. Springer International

Vickers D, Mahrt L (1997) Quality control and flux sampling problems for tower and aircraft data. Journal of atmospheric and oceanic technology 14(3):512–526

Weinstock J (1981) Energy dissipation rates of turbulence in the stable free atmosphere. Journal of the Atmospheric Sciences 38(4):880–883

Wilson JM, Venayagamoorthy SK (2015) A Shear-Based Parameterization of Turbulent Mixing in the Stable Atmospheric Boundary Layer. Journal of Atmospheric Sciences 72:1713–1726

Yadav AK, Raman S, Sharan M (1996) Surface layer turbulence spectra and dissipation rates during low winds in tropics. Boundary-Layer Meteorology 79(3):205–223

Zilitinkevich SS, Elperin T, Kleeorin N, Rogachevskii I, Esau IN (2013) A Hierarchy of Energy- and Flux-Budget (EFB) Turbulence Closure Models for Stably-Stratified Geophysical Flows. Boundary-Layer Meteorol 146:341–373